Inkjet-printed high-Q nanocrystalline diamond resonators

Sartori, André F.; Belardinelli, Pierpaolo; Dolleman, Robin J.; Steeneken, Peter G.; Ghatkesar, Murali K.; Buijnsters, Josephus G.

DOI
10.1002/smll.201803774

Publication date
2019

Document Version
Final published version

Published in
Small

NANO · MICRO small
www.small-journal.com

Inkjet-Printed High-*Q* Nanocrystalline Diamond Resonators

André F. Sartori, Pierpaolo Belardinelli, Robin J. Dolleman, Peter G. Steeneken, Murali K. Ghatkesar,* and Josephus G. Buijnsters**

Diamond is a highly desirable material for state-of-the-art micro-electromechanical (MEMS) devices, radio-frequency filters and mass sensors, due to its extreme properties and robustness. However, the fabrication/integration of diamond structures into Si-based components remain costly and complex. In this work, a lithography-free, low-cost method is introduced to fabricate diamond-based micro-resonators: a modified home/office desktop inkjet printer is used to locally deposit nanodiamond ink as ⌀50–60 µm spots, which are grown into ≈1 µm thick nanocrystalline diamond film disks by chemical vapor deposition, and suspended by reactive ion etching. The frequency response of the fabricated structures is analyzed by laser interferometry, showing resonance frequencies in the range of ≈9–30 MHz, with *Q*-factors exceeding 10^4, and ($f_0 \times Q$) figure of merit up to ≈2.5×10^{11} Hz in vacuum. Analysis in controlled atmospheres shows a clear dependence of the *Q*-factors on gas pressure up until 1 atm, with $Q \propto 1/P$. When applied as mass sensors, the inkjet-printed diamond resonators yield mass responsivities up to 981 Hz fg^{-1} after Au deposition, and ultrahigh mass resolution up to 278 ± 48 zg, thus outperforming many similar devices produced by traditional top-down, lithography-based techniques. In summary, this work demonstrates the fabrication of functional high-performance diamond-based micro-sensors by direct inkjet printing.

1. Introduction

Nanocrystalline diamond (NCD) is the ultimate material for the fabrication of radio-frequency (RF) micro/nanoelectromechanical (MEMS/NEMS) devices, such as resonators and switches for wireless communication systems, as it promises high operating frequency in the GHz range, as well as narrow bandwidth (high *Q*-factor) and low phase noise.[1–3] This is thanks to diamond's excellent material properties, such as high Young's modulus (up to ≈10^6 N mm^{-2}), high acoustic velocity (≈1.8×10^4 m s^{-1}),[3] low thermoelastic damping, high thermal conductivity (>2000 W m^{-1} K^{-1}), and low thermal expansion coefficient (≈10^{-6} K^{-1} at 300 K).[4] The feasibility of using NCD for high-performance MEMS resonators has already been demonstrated in a range of devices, including cantilever beams,[5,6] tuning forks,[7] rings,[8] disks,[9–11] and spheres.[12] In particular, NCD MEMS structures that resonate with whispering gallery modes (WGM), such as disks and spheres, have shown much lower anchor losses and higher ($f_0 \times Q$) figure of merit.[3,11] However, despite the recent progress, adding diamond structures into integrated circuits for a complete functional device remains a challenge. The current limitations relate to the difficulty in combining NCD with other microfabricated structures, mostly due to nanodiamond seeding requirements, but also due to the harsh environment during chemical vapor deposition (CVD) of the NCD film, as well as mechanical issues caused by intrinsic stress in the film.[13] Nanodiamond seeding in particular suffers from the process not being selective, i.e., instead of diamond being deposited and grown only where it is required on the device, most established methods consist of dispersing nanodiamond over a large substrate by, e.g., dip-coating, drop-casting, or spin-seeding, prior to film growth by CVD.[14] The grown NCD film needs then to be patterned by traditional photo-/e-beam lithography and lift-off techniques, which add substantial complexity and cost of fabrication. As a solution to circumvent low seeding density and plasma uniformity issues during growth of the NCD layer, Lebedev et al. proposed wafer-to-wafer bonding of pregrown NCD films onto another wafer to fabricate NCD disk resonators with high *Q*-factors (i.e., $Q > 10^3$).[9] This technique however did not remove the need to pattern the diamond after it was bonded onto the wafer. Possas et al. demonstrated the fabrication of NCD cantilever beams by patterning the nanodiamond seeding layer by means of sacrificial metal layer and etching,[15] but still top-down patterning by lithography was required. Akgul et al. reported *Q*-factors of the order of 7×10^4 for on-chip NCD disk resonators which required up to five masking/etching steps.[11] Yang et al., on the

Dr. A. F. Sartori, Dr. P. Belardinelli, Dr. R. J. Dolleman, Prof. P. G. Steeneken, Dr. M. K. Ghatkesar, Dr. J. G. Buijnsters
Department of Precision and Microsystems Engineering
Delft University of Technology
Mekelweg 2, 2628 CD Delft, The Netherlands
E-mail: A.FrotaSartori@tudelft.nl; M.K.Ghatkesar@tudelft.nl; J.G.Buijnsters@tudelft.nl
Dr. R. J. Dolleman, Prof. P. G. Steeneken
Kavli Institute of Nanoscience
Delft University of Technology
Lorentzweg 1, 2628 CJ Delft, The Netherlands
The ORCID identification number(s) for the author(s) of this article can be found under https://doi.org/10.1002/smll.201803774.

DOI: 10.1002/smll.201803774

other hand, applied focused ion beam (FIB) in the fabrication of NCD nanoresonators in order to avoid the drawbacks of e-beam lithography.[16] However, FIB is not a high-throughput and low-cost manufacturing process. Overall, not much focus is given to reducing the cost and complexity of microfabricated diamond MEMS/NEMS, but rather given to device design,[11,15] structure,[13] actuation mechanisms,[2] sensing,[17–20] and other phenomena.[21,22] Therefore, new more efficient and cost-effective solutions are necessary. In this work, we propose inkjet printing.

Inkjet printing is a very attractive patterning/fabrication technique,[23] because it allows the selective deposition of a fluid directly where it is required on a given 2D or 3D structure; it is maskless, it can meet the precision requirements for fabrication of submillimeter devices over large areas, it is compatible with large-scale manufacturing, and it is low-cost. These features also enable rapid prototyping of devices. Inkjet printing has been applied successfully in diverse fields, particularly in the fabrication of flexible electronics,[24–27] wearable[28,29] and microfluidic devices,[30,31] and many others, but not for patterning and fabrication of diamond devices.

The proof-of-principle of inkjet printing of diamond particles has been shown before, first by Fox et al. in 2000,[32] and later by others.[33–35] In those studies, the dispensing of diamond ink itself, and the shape and morphology of the diamond structures grown out of the printed patterns were demonstrated. The achieved printing resolution was rather low (>100 µm in lateral size), and the seeding (or nucleation) density and uniformity were often too low to enable growth of reproducible NCD structures. Thus, functional inkjet-printed NCD MEMS devices have not been realized up to now.

In this work, we demonstrate the direct fabrication of NCD micro-disk resonator structures onto a Si substrate, through the selective/local printing of water-based nanodiamond ink using a modified off-the-shelf desktop inkjet printer[36] (see **Scheme 1** below). With control of each individual nozzle of the printer head, we were able to increase the resolution and reproducibility of the printed structures and fabricate an array of NCD micro-disk resonators with dimensions down to ⌀50–60 µm without photolithography or lift-off steps, and across an area of the order of cm^2. The frequency response of the fabricated resonators was measured by laser interferometry upon optothermal actuation. The resonant frequencies and *Q*-factors were determined both in vacuum and in controlled atmosphere (He, N_2, Kr, and SF_6), and compared with values reported in the literature for NCD micro-disk resonators fabricated by conventional top-down techniques. We demonstrate as well the application of the inkjet-printed NCD resonators as mass sensors with the deposition of a thin Au layer by e-beam evaporation. The experimental data was supported and complemented by finite element method (FEM) simulations, as to determine the mode shapes and physical parameters of the resonators.

2. Results and Discussion

2.1. Printing of NCD Disks

In order to demonstrate the resolution limit and accuracy of our inkjet printing method with the water-based nanodiamond ink, the printer was set to produce the smallest droplets (see Experimental Section) through each individually addressed nozzle. Then, a "TU Delft" bitmap was loaded and the pattern was printed onto a silicon wafer positioned under the printer head. The printed outcome of a representative droplet is shown in **Figure 1**a,b. It can be seen that, after the water evaporated, the droplets left behind well-defined circular areas containing a high density of diamond nanoparticles. The bright contrast in the scanning electron microscopy (SEM) images corresponds to areas with higher density of nanodiamond. The printed disks resulted very uniform in shape, as indicated by the reference dashed line, with a diameter of ≈38 µm and some striations around the edge (indicated by the arrowhead). This size matches the smallest droplet size previously obtained with normal ink on a hydrophobic glass surface, using the same printer.[36] A radial contrast gradient can also be seen, where rings of lower and higher contrast alternate toward the edge. The striations can be attributed to capillary effects at the edge of the droplet, while the contrast gradient is caused by a long-range inhomogeneous distribution of the diamond nanoparticles similar to a "coffee stain" effect.[37,38] Figure 1b shows a high-resolution SEM image of the center of the printed disk, where small agglomerates of diamond nanoparticles can be seen dispersed across the surface. This image is representative of many nanodiamond disks printed by our technique and shows a distribution of particles very similar to what is observed with standard spin-seeding procedures for diamond thin-film growth.[39] Compared to our own spin-seeding technique, however, the printed nanodiamond shows stronger agglomeration of the nanoparticles (see Figure S1 in the Supporting Information for comparison), which is caused by the ink being water-based instead of ethanol-based. The higher surface tension[40,41] of water (≈72 mN m^{-1} at 20 °C) compared to ethanol (≈22 mN m^{-1} at 20 °C) contributes to the agglomeration. The choice of water over ethanol was necessary due to its higher viscosity, in order not to leak through the printer nozzles. Nonetheless, from Figure 1b, we estimated a high seeding density of the order of ≈10^{10} cm^{-2}, which is a desirable order of magnitude to enable the growth of fully closed thin-films of only 100–200 nm thickness, with good adhesion to the substrate and low surface roughness.[42,43]

After printing, the sample was loaded into the hot-filament chemical vapor deposition (HFCVD) chamber for diamond

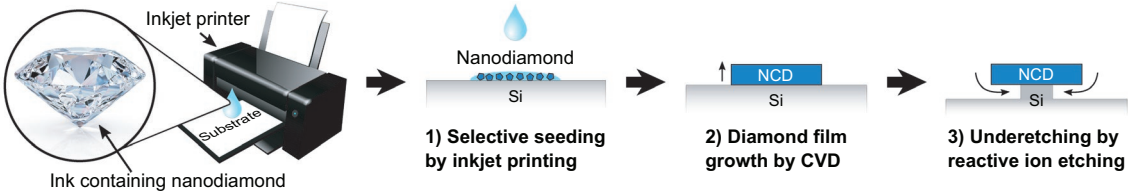

Scheme 1. Fabrication process of NCD micro-disk resonators by inkjet printing.

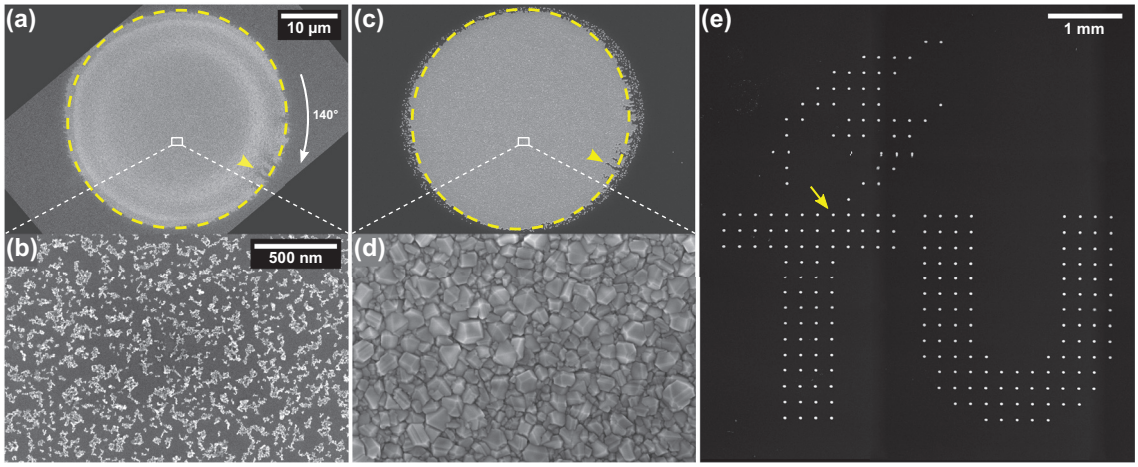

Figure 1. SEM images of a,b) printed and c–e) grown diamond disks (no underetching). a) Printed droplet consisting of diamond nanoparticle clusters, shown in detail in (b). The image was rotated by 140° to match (c). c) Same droplet after growth by CVD into a closed NCD film of ≈135 nm thickness, shown in detail in (d). e) Stitched SEM image of many NCD disks produced on the Si substrate. The yellow arrow in (e) marks the position of the disk shown in (a)–(d). The yellow arrowheads in (a) and (c) mark the same feature for reference.

thin-film growth for 30 min at 725 °C, in an atmosphere of 0.5% CH_4 in H_2 (300 sccm total flow) at 10 mbar. The low growth rate promoted by low methane concentration was chosen for better control of the film thickness. The complete "TU Delft" pattern of diamond thin-film disks can be seen in Figure S2 in the Supporting Information. Details of one disk can be seen in Figure 1c,d. The SEM images show a fully closed NCD film after growth, with sharply defined edges following the original seeding pattern (see arrowhead and reference dashed line). An outer rim of sparse diamond crystals can also be seen, which was not visible before growth. They arise likely from in-plane stretching of the droplet while it is impacting the surface during printing, which causes a few diamond nanoparticles to be left behind before the droplet conformed to a more stable hemispherical shape. A closer look reveals that the outer rim is slightly stretched along the horizontal direction. This coincides with the printing direction and, thus, the deformation arises from the droplet carrying also lateral velocity. Along this direction, the outer rim adds further ≈4 µm in diameter to the disk, to a total of ≈42 µm.

A topography map of the disk was obtained by 3D optical profilometry and is shown in Figure S3a (Supporting Information). It can be clearly seen there that the diamond film resulted very flat, smooth, and homogeneous, which is due to the high density and homogeneity of the dispersed diamond nanoparticles after printing. The low NCD film thickness of ≈135 nm also contributes to the smoothness of the diamond disk. At closer inspection, an inner ring of slightly higher thickness can be observed sitting just underneath the arrowhead. It correlates with the inner ring of brighter contrast seen in Figure 1a, which is an area where a higher density of diamond nanoparticles was deposited. Due to the "coffee stain" effect, the thickness of the diamond film became slightly higher in that region. The additional outer rim composed of sparse diamond particles observed in Figure 1c cannot be seen in the optical image due to limited resolution of the optical setup. In Figure S3b (Supporting Information), a Raman mapping of a random disk on the same substrate is shown. The most prominent features in the Raman spectra are the Si peak at ≈520.7 cm^{-1} (not shown) and the well-known signature peak for diamond at ≈1332 cm^{-1}. Due to the selected growth conditions with low methane concentration, the diamond film contains low sp^2 carbon content, and therefore the D and G bands[44] are weak.

2.2. Fabrication of NCD Disk Resonators

Here, we apply our inkjet printing technique in the fabrication of NCD micro-disk resonators. In the subsequent sections, the fabricated resonators will be demonstrated as pressure/gas and mass sensors.

The target dimensions of the devices (i.e., diameter and thickness of the NCD disk, as well as the diameter of the Si supporting stem) were chosen, with help of COMSOL simulations, such that the resonance frequencies of the NCD disk resonators would be of the order of ≈10 MHz, which is comfortably measurable with our tools. The following dimensions were chosen: ≈50 µm for the disk diameter, ≈1 µm for the disk thickness and ≈25 µm for the stem diameter.

In order to achieve the larger disk diameter, the NCD disks were fabricated as described earlier, but with medium droplet size setting instead of small (see Experimental Section for more details). After that, the NCD disks were grown by HFCVD for 1 h at 725 °C, 10 mbar, 300 sccm H_2, and 6 sccm CH_4. As a last step, the sample was subjected to reactive ion etching (RIE) for the underetching of the Si substrate in two consecutive runs of 3 + 6 min, and then acid-cleaned. An overview of the fabricated array of NCD micro-disk resonators is shown in **Figure 2**.

Upon observation, one can see that the NCD disks are fairly uniform in shape, with ≈50 µm being the smallest diameter and ≈60 µm the largest. By measuring seven arbitrary disks in the area shown in Figure 2a, an estimation of the average diameter resulted in 54 ± 4 µm. The NCD thickness is consistently around 1.2 ± 0.1 µm.

The largest variations in device dimensions come from the supporting Si stem, with diameters ranging from ≈10 µm for

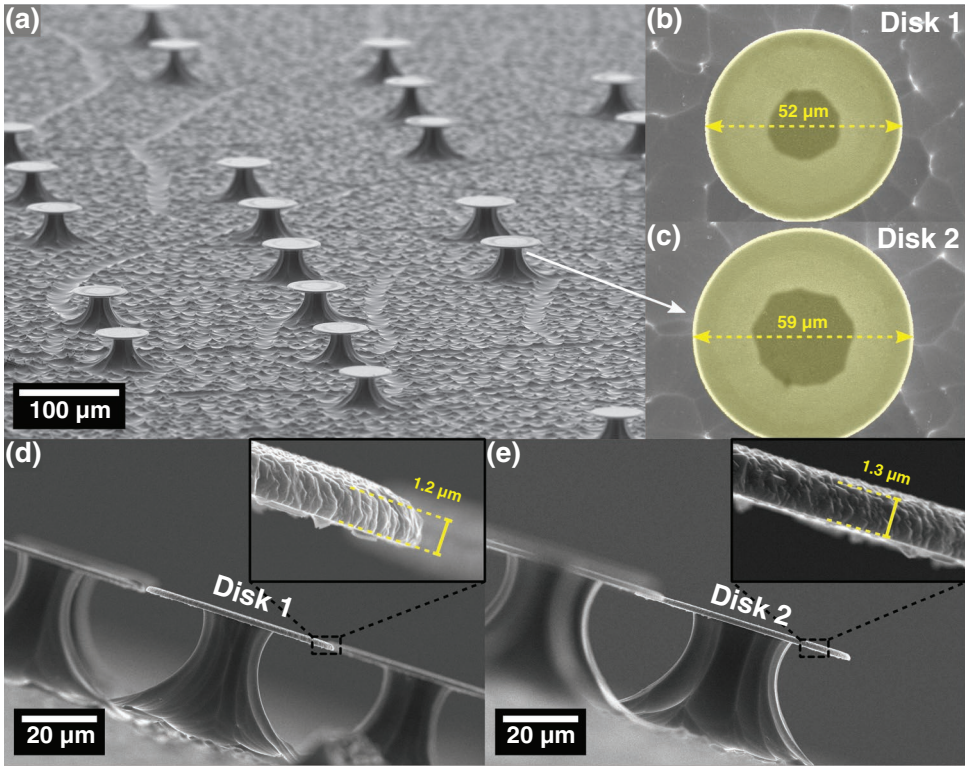

Figure 2. SEM images of suspended NCD micro-disk resonators fabricated by inkjet printing. a) Overview image showing several devices. b,c) Top-view images of two randomly selected disks. The false yellow color highlights the NCD disks. The inner regions with darker contrast correspond to the supporting Si stem underneath the disks. d,e) Tilted side-view of the same disks shown in (b) and (c), respectively.

the smallest disks, up to ≈25 µm for the largest disks. Statistics from the same seven disks resulted in an average stem diameter of 19 ± 6 µm. The variation arises due to two reasons: 1) size of the NCD disk and 2) inhomogeneity of the etch rate across the sample during RIE, with the devices near the edge of the Si substrate undergoing higher etch rate than the devices farther away from the edges. It is also clear from Figure 2b,c in particular that the stems are not uniformly round, but are rather faceted, which is a consequence of the chosen etching parameters. Finally, it can be seen from Figure 2d,e that the NCD disks remain very flat after being suspended, which is an indication of low residual stress in the diamond film. Added to the fact that none of the disks on the entire Si substrate collapsed or delaminated at any stage during or after RIE, our results show good adhesion between the NCD film and the substrate, thanks to the adequate growth conditions and seeding quality. The latter, in particular, is comparable to that of previously reported NCD films which successfully withstood reciprocating sliding tests against ceramic ball counter-bodies with Hertzian contact pressures up to 1.4 GPa, without delamination or spallation.[43,45]

Figure 3a,b shows, respectively, optical microscopy and optical profilometry images of disk 1. An outer ring can be clearly discerned (see white arrows), which corresponds to the "coffee stain" effect in the distribution of the diamond nanoparticles during evaporation of the water-based ink. A larger density of nanoparticles along the ≈4 µm wide outer rim led to slightly thicker NCD film after growth. The rim is ≈0.2 µm higher than the inner surface of the disk for the ≈1.2 µm thick NCD film. Figure 3c shows Raman spectra taken at the positions on the disk indicated by i) and ii), i.e., above the Si stem and near the edge, respectively. The spectra feature the characteristic diamond one-phonon line at ≈1332 cm^{-1}, as well as both the D and G bands,[44,46] which indicate sp^2 carbon content in the diamond film and confirm the nanocrystalline quality of the material.

2.3. Frequency Response of NCD Micro-Disk Resonators in Vacuum

The measured resonance frequencies of two selected NCD micro-disk resonators are shown in **Figure 4**, along with the mode shapes obtained from FEM simulations. **Table 1** lists the physical parameters estimated from fitting the models of each disk to the experimental data. The results show that the NCD disks operate at relatively high frequencies, starting at around 9–10 MHz for the fundamental mode, up to around 30 MHz for the highest detected mode. The resonance frequencies vary between the two devices, however the mode shapes are qualitatively very similar. In total, seven resonance frequencies were measured with disk 1, whereas eight were measured with disk 2. FEM simulations indicated an additional resonance frequency for disk 1 and two additional ones for disk 2, which were not detected experimentally, and thus we numbered the modes according to the simulations. Resonance coupling[47] can be

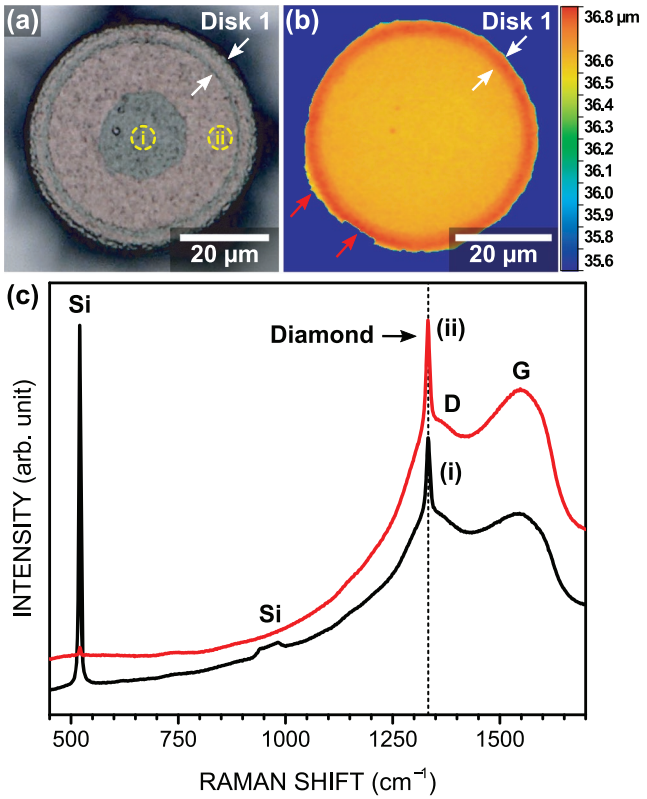

Figure 3. a) Optical microscopy image of NCD micro-disk resonator (same disk as in Figure 2b). The indices i) and ii) mark the positions where Raman spectra were taken. b) Optical profilometry image of the same disk shown in (a). The white arrows highlight the outer rim of the disk. The red arrows mark edge artefacts. c) Raman spectra of the disk, measured at two spots: i) above the stem, and ii) near the edge.

clearly observed between the 5th–6th and 7th–8th modes in the case of disk 1, and between 7th–8th modes in the case of disk 2. The 2nd–3rd modes for disk 1 and the 1st–2nd modes for disk 2 also appear to be coupled (see Figure S4 in the Supporting Information for additional data). Overall, it can be concluded that the observed differences arise mostly due to variations in size and shape of the disks, as a consequence of slight variations in droplet size and shape from the inkjet printing process, and also due to the formation of irregular stem shapes from the reactive ion etching conditions.

Such irregularities are difficult to model in detail. Despite our best efforts, there were still visible deviations between the fitted/theoretical resonance frequencies (red dashed lines in Figure 4) and the measured values for certain modes, particularly the 5th and 6th modes for disk 1, and the 5th, 6th, and 9th modes for disk 2, although the correspondence was better in the case shown in Figure S4 (Supporting Information). Nonetheless, the deviations were always within 10% (see Table S2 in the Supporting Information). The overall good numerical agreement and the correspondence between the mode shapes of the two disks, indicate that the models describe the experimental results quite well both quantitatively and qualitatively.

Figure 5 shows the relationship between the quality factors and the resonance frequencies, and compares the obtained values with data from Lebedev et al. (wafer-bonded NCD on Si).[9] It can be seen that the inkjet-printed NCD micro-disk resonators display consistently high Q-factors of up to $\approx 1 \times 10^4$ for both disks, which can be understood as a consequence of the chosen dimensions (i.e., lower clamping losses due to the formation of whispering gallery modes), but mostly of material and device quality. The obtained Q-factors also surpassed that of the single crystal diamond nanomechanical resonator reported by Zalalutdinov et al.,[48] as well as the torsional NCD nanoresonator fabricated by FIB reported by Yang et al.[16] The simulation data in Table 1 and Table S1 (Supporting Information) show that the expected Young's modulus is around 600 GPa, which is consistent with values reported for NCD.[43,49] Thus, despite the small variations in device dimension (e.g., disk diameter and roundness, stem diameter and shape) between the disks, the inkjet-printed NCD micro-disk resonators perform remarkably well. Figure 5 also shows how acid-cleaning the devices after RIE (triangle symbols) improved the Q-factors, likely as a consequence of debris and residuals produced by the RIE step being removed.

2.4. Frequency Response of NCD Micro-Disk Resonators in Controlled Atmosphere

The behavior of the NCD micro-disk resonators was also characterized in controlled atmosphere, using gases with low to high density: He (0.179 g L^{-1}), N_2 (1.250 g L^{-1}), Kr (3.749 g L^{-1}), and SF_6 (6.17 g L^{-1}). **Figure 6** shows the Q-factors of the 2nd, 3rd and 4th modes of disk 1, measured while sweeping the pressure from 10 → 1000 → 10 mbar for each gas. The data was then fitted to the following equation

$$Q_{exp} = a/(P+b) \tag{1}$$

where Q_{exp}, P, a, and b are the fitted pressure-dependent Q-factors, the pressure and the fitting coefficients, respectively. This expression models the pressure-dependent Q-factor, which includes contributions from intrinsic losses and molecular damping, such that[50]

$$\frac{1}{Q_{exp}} = \frac{1}{Q_i} + \frac{1}{Q_m} \tag{2}$$

where Q_i is the Q-factor only due to intrinsic losses, and Q_m is the Q-factor only due to molecular damping. It follows that, for $P \ll b$, $Q_{exp} \approx Q_i = a/b$, and thus $Q_m = a/P$, with the constant a given by[51,52]

$$a = \left(\frac{\pi}{2}\right)^{3/2} \rho d f_0 \sqrt{R_0 T / M_0} \tag{3}$$

where ρ is the density of the resonator, d is its thickness, f_0 is the mode frequency, R_0 is the ideal gas constant, T the absolute temperature, and M_0 the molar mass of the respective gas. The constant b marks the crossover point where Q_m becomes smaller than Q_i as the pressure increases, and the molecular damping mechanism better describes the Q-factor than intrinsic losses. Thus, using Equations (1) and (3), the

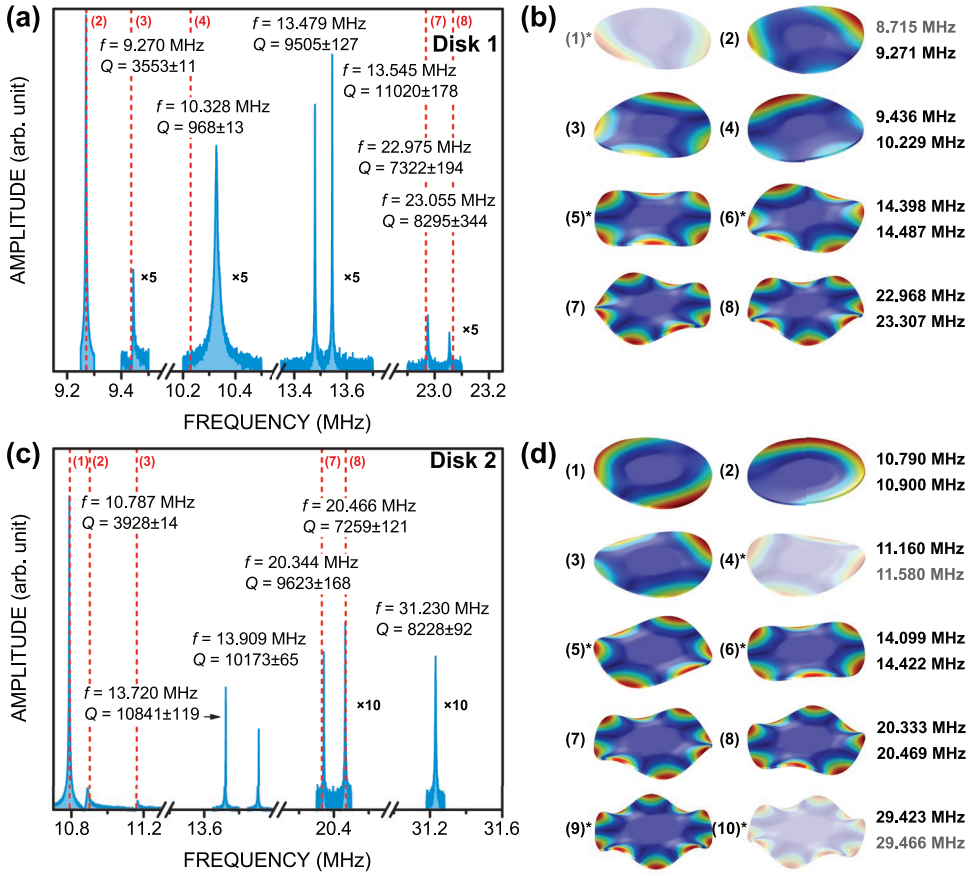

Figure 4. Resonance frequencies, *Q*-factors and mode shapes of the NCD micro-disk resonators fabricated by inkjet printing. a,b) Response from disk 1 shown in Figure 2b,d. c,d) Response from disk 2 shown in Figure 2c,e. The fitted mode shapes marked by (*) deviate more from the experimental values (see Table S2 in the Supporting Information), and thus fall outside the axis range in the plots. The 1st mode from disk 1 and the 4th and 10th modes from disk 2 were not detected experimentally. For better visualization, the amplitude of some peaks was scaled by either ×5 or ×10, as indicated. Additional data measured before acid cleaning are shown in Figure S4 and Table S1 in the Supporting Information for comparison.

resonance regime can be characterized, and the experimental results compared with theory. The fitted curves are shown in Figure 6 as black lines matching their respective modes, and the fitted coefficients are listed in **Table 2**.

Upon analysis, several things can be concluded: 1) the heavier gases led to stronger damping, as seen from the steeper decrease of the *Q*-factors, which is expected due to larger momentum transfer from the heavier molecules; 2) a transition from molecular damping to viscous damping[52,53] occurs as the pressure approaches 1 atm, as seen by the deviation of the measured *Q*-factors from Q_{exp} particularly for the 2nd mode; 3) despite the transition to viscous damping occurring at lower pressures for the heavier gases, as indicated by the Knudsen number, Kn (dashed vertical line),[54] the

Table 1. Parameters from FEM simulation of disk 1 and disk 2, determined for the measured frequency response shown in Figure 4.

Disk #	d [μm]	ρ [kg m^{-3}]	E [GPa]	A_{tot} [μm^2]	A_{sus} [μm^2]	m_{tot} [pg]	m_{sus} [pg]
1	1.11	3300	595	2127.0	1842.8	7.7913	6.7503
2	1.16	3320	611	2711.0	2145.5	10.441	8.2628

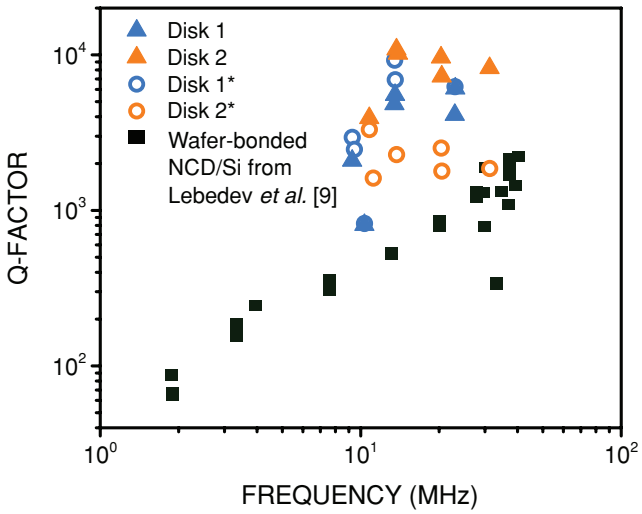

Figure 5. Quality factors from the inkjet-printed NCD micro-disk resonators from this work compared with the values reported by Lebedev et al. for wafer-bonded NCD disk on Si.[9] The corresponding ($f_0 \times Q$) figures of merit of the present NCD resonators are shown in Figure S5 (Supporting Information). (*) Measured before acid cleaning, with the complete analysis given in Figure S4 and Table S1 in the Supporting Information.

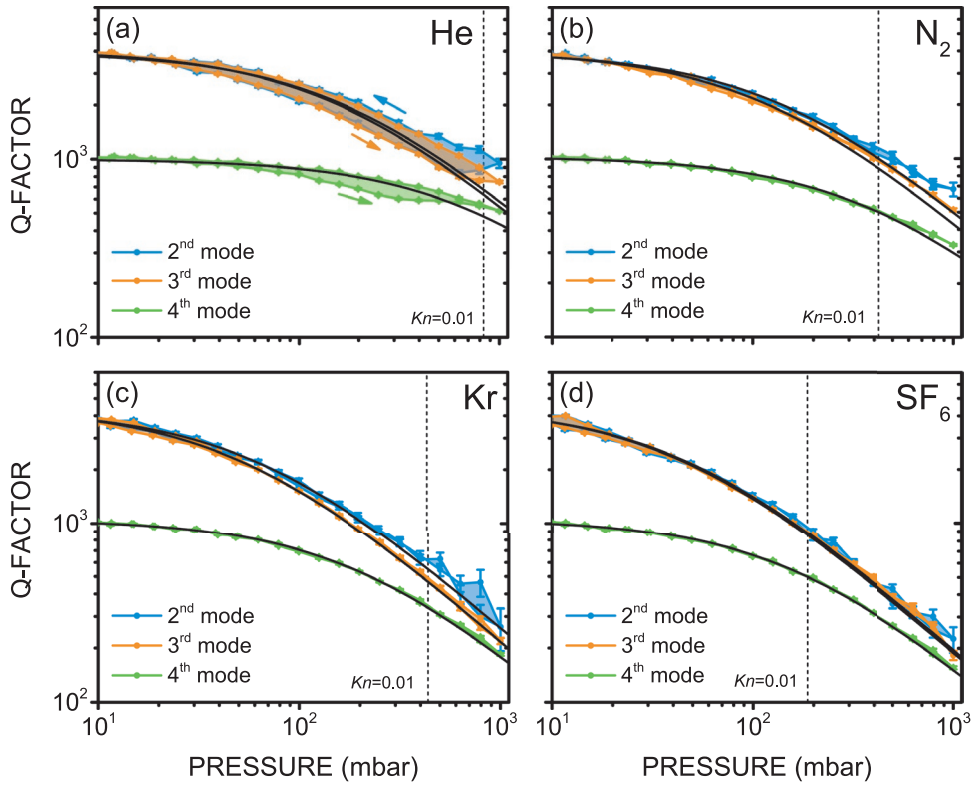

Figure 6. Pressure dependence of the resonance quality factor of NCD micro-disk resonator 1 in a) helium, b) nitrogen, c) krypton, and d) sulfur hexafluoride. The data points are shown in blue, orange, and green, respectively for the 2nd, 3rd, and 4th modes. The black curves are their respective fits to Equation (1). The devices underwent an acid cleaning procedure beforehand, as described in the Experimental Section. The Knudsen number was estimated assuming the difference between the NCD disk radius and the Si stem radius as an equivalent beam width in the case of a rectangular cantilever. Kn marks the point where the gas behaves like an incompressible fluid and viscous damping dominates. The values are given in Table 2.

Q-factors still follow very closely the a/P law in this regime. This is unlike observations with cantilever beam resonators, where the *Q*-factor in the viscous damping regime becomes virtually independent of pressure.[50–53] However, the frequency downshifts with increasing *P*, as shown in Figure S6 in the Supporting Information, which confirms increasing damping due to increasing gas density. On the other hand, the structure of our device prevents it from undergoing squeeze-film damping,[55] as the NCD disk is ≈35.6 µm above the Si surface (see Figure 3b), which is larger than 1/3 of the width of the suspended ring-shaped area of the NCD disk, i.e., ≈16.5 µm.[51] Finally, it can be seen that the 4th mode suffers lower damping than the 2nd and 3rd modes for all gases, with the viscous damping regime also setting at higher pressures. This behavior is similar to the observation by Gavan et al. for cantilever beams,[53] where a general trend of the *Q*-factors being less sensitive to pressure for the higher modes was reported, and explained as a consequence of smaller displacements.

Compared with a similar NCD resonator reported by Yoshikawa et al. (Q_{min} = 85 at 2.2 MHz, Q_{max} = 190 at 7.36 MHz in air),[2] our inkjet-printed NCD resonator performed rather well in atmospheric conditions, showing consistently higher *Q*-factors, with values above 200 in N_2 atmosphere, although in that work the NCD resonators likely suffered from squeeze-film damping due to the capacitive actuation mechanism.

2.5. Mass Sensing Performance in Vacuum

The responsivity of the NCD micro-disk resonator 1 for mass sensing was also evaluated, by measuring the frequency shift and *Q*-factor before and after the deposition of a thin layer of gold on top of it. All measurements were performed within 24 h and the sample was left in the interferometer's vacuum chamber overnight after Au evaporation, in order to minimize the risk of surface contamination from air before the new measurements. Additional data from disk 2 is given in Figure S7 in the Supporting Information. A nominal value of 2.5 nm for the thickness of the Au layer was obtained from the quartz microbalance installed in the e-beam evaporator. However, FEM simulations revealed that the observed frequency shift corresponds to an added mass of 67.5 fg onto the NCD disk 1, of which 58.5 fg is the quantity on the suspended region of the resonator's top surface. This mass is equivalent to a gold layer thickness of ≈1.64 nm. Thus, from the measured frequency shifts shown in **Figure 7**, a responsivity to mass change of 664 Hz fg^{-1} was determined for the 2nd mode, and 981 Hz fg^{-1} for the 6th mode. An estimation of the mass

Table 2. Curve fitting parameters of the data shown in Figure 6. $Q_m \times P$ corresponds to the theoretical coefficient a given in Equation (3), and thus $(Q_m \times P)/a$ is the ratio between the theoretical value (with d and ρ from FEM simulation) and the experimentally obtained one. The uncertainties of d and ρ if estimated from Equation (3) are given in Table S3 in the Supporting Information.

Gas	Mode	$a \times 10^{-5}$ [mbar]	b [mbar]	f_0 [MHz]	$Q_i = a/b \times 10^{-3}$	$(Q_m \times P) \times 10^{-5}$ [mbar]	$(Q_m \times P)/a$	$P_{Kn=0.01}$ [mbar]
He	2nd	6.81 ± 0.44	173 ± 14	9.270	3.95 ± 0.40	5.279	0.77	835.34
He	3rd	6.28 ± 0.33	155 ± 10	9.444	4.04 ± 0.34	5.378	0.86	835.34
He	4th	7.68 ± 0.54	770 ± 61	10.328	1.00 ± 0.11	5.881	0.77	835.34
N_2	2nd	5.70 ± 0.17	144.5 ± 5.5	9.270	3.94 ± 0.19	1.995	0.35	426.19
N_2	3rd	4.80 ± 0.12	120.3 ± 3.8	9.444	3.99 ± 0.16	2.032	0.42	426.19
N_2	4th	4.168 ± 0.081	405.6 ± 9.1	10.328	1.027 ± 0.031	2.222	0.53	426.19
Kr	2nd	2.742 ± 0.078	63.1 ± 2.5	9.270	4.35 ± 0.21	1.153	0.42	435.71
Kr	3rd	2.275 ± 0.052	51.0 ± 1.5	9.444	4.46 ± 0.18	1.175	0.52	435.71
Kr	4th	2.140 ± 0.022	203.6 ± 2.6	10.328	1.051 ± 0.017	1.285	0.60	435.71
SF_6	2nd	2.047 ± 0.072	45.4 ± 2.4	9.270	4.51 ± 0.28	0.8736	0.43	186.67
SF_6	3rd	1.970 ± 0.058	43.4 ± 1.9	9.444	4.53 ± 0.24	0.8900	0.45	186.67
SF_6	4th	1.761 ± 0.020	167.2 ± 2.4	10.328	1.053 ± 0.019	0.9732	0.55	186.67

resolution[48] from $\delta m \approx m_{sus}/Q$, with m_{sus} being the mass of the resonator (see Table 1), yields 3.2 and 1.2 fg, respectively for the two modes. Assuming the Q-factor at 1 atm in N_2, the mass sensitivity would result 28.2 fg for the 2nd mode. In comparison, Cagliani et al. demonstrated mass sensors based on poly-Si micro-disk resonators with resolution down to 15 fg, considering a frequency rms noise of 64 Hz.[56] Possas et al. demonstrated responsivities down to ≈196 Hz ng^{-1} for NCD micro-cantilevers,[17] while Bongrain et al. reported 227.4 Hz ng^{-1} and mass resolution of 0.86 pg for a similar device.[19] The ultimate mass resolution achieved by our NCD micro-disk resonator was estimated from the Allan deviation[57,58] measurements shown in Figure S8 (see Supporting Information). This analysis resulted in the smallest detectable distributed mass changes of 6.53 ± 0.73 and 3.36 ± 0.58 ag for the 2nd and 6th modes, respectively. With the effective masses, m_{eff}, determined by FEM simulations, the ultimate modal mass resolution resulted in 2.16 ± 0.24 and 0.278 ± 0.048 ag for the same modes. These are, to the best of our knowledge, the lowest values reported for NCD resonators, and demonstrate the potential of inkjet printing for the fabrication of sensitive, yet low-cost NCD-based environmental sensors and biosensors.

3. Conclusion

In summary, this work demonstrated the application of inkjet printing for the bottom-up, lithography-free fabrication of nanocrystalline diamond-based micro-resonators. The technique, which uses a commercial, off-the-shelf desktop printer, enabled the fabrication of diamond disk structures down to ≈38 µm in diameter, with good uniformity, reproducibility, and high density of diamond nanoparticles. By controlling the printer settings, larger nanocrystalline diamond disks with 54 ± 4 µm in diameter and ≈1 µm thick were fabricated and applied as micro-resonators after partial underetching of the Si substrates. Analysis of the frequency response showed consistently high Q-factors (>10^3) exceeding 10^4, and ($f_0 \times Q$) figures of merit up to ≈2.5×10^{11} Hz in vacuum, which are higher than for other reported diamond disk resonators produced by conventional lithography-based techniques.[2,9] Even higher performances can be expected with further optimization of the NCD growth conditions, e.g., by adding oxygen to the gas mixture during CVD,[59] to improve material properties and reduce intrinsic losses.

The frequency response of the NCD micro-disk resonators was also analyzed in He, N_2, Kr, and SF_6 from 10 to 1000 mbar, showing that the 4th mode undergoes less dissipation due to molecular damping and weaker pressure dependence than the 2nd and 3rd modes. The Q-factors also remained pressure-dependent throughout the measured range, in all cases, with a ≈$1/P$ dependency also in the viscous regime, despite the heavy gases. This result enables the use of the inkjet-printed NCD micro-disk resonators as sensitive pressure sensors in the whole measured pressure range.

In a last step, the inkjet-printed NCD resonators were applied for the mass sensing of gold after e-beam evaporation, in order to estimate the mass sensitivity of the fabricated devices. The analysis of the 2nd and 6th modes yielded high responsivities of 664 and 981 Hz fg^{-1}, respectively, which are orders of magnitude higher than previously reported values pertaining to NCD cantilevers and poly-Si resonators.[17,19,56] The analysis of the Allan deviation showed that our devices displayed ultralow distributed mass resolution of less than 10 ag, and ultimate modal mass resolution below 1 ag.

Thus, we demonstrated that inkjet printing is a simple and low-cost route for the fabrication of functional diamond-based micro-devices/sensors, such as environmental sensors, biosensors or mass sensors, which can compete with, and even outperform, equivalent devices produced by costly, traditional top-down lithography-based techniques. By tuning the CVD growth conditions, ultrananocrystalline (UNCD) and microcrystalline diamond (MCD) resonators can also be fabricated by inkjet printing. With further optimization of the nanodiamond ink's viscosity, the regularity of the printed nanodiamond disks can be further improved while still preventing clogging of the printer nozzles. Combined with the addition of

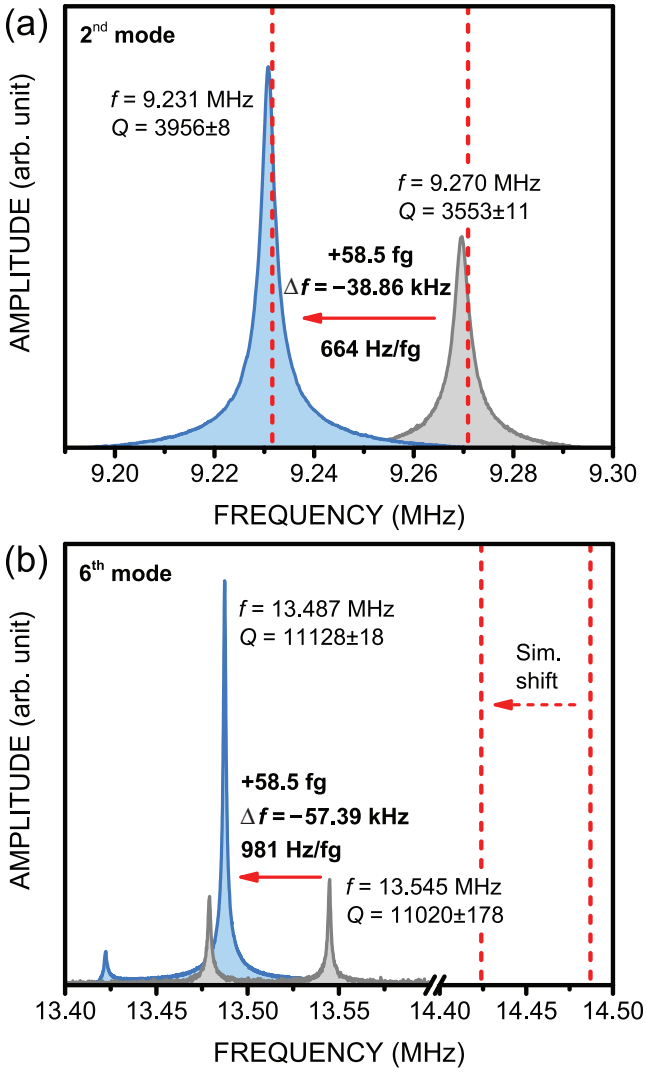

Figure 7. Frequency shift with additional mass of evaporated Au onto disk 1, measured in vacuum. a) 2nd mode. b) 6th mode. The dashed lines correspond to the estimated resonance frequencies by FEM simulations. Although the absolute positions for the 6th mode do not match, the estimated frequency shift is the same as the experimental result in both cases.

a movable stage for the substrate, the printing of more complex patterns will enable fast and low-cost production of a wide range of diamond-based micro-devices, which is the aim for future work.

4. Experimental Section

Printer Setup: The printing technique used in the present study was based on the work carried out earlier in our department,[36] where a commercial desktop printer, Epson Stylus SX235W, was hacked in order to gain access to the individual nozzles (⌀75 µm) and single droplet dispensing. In the present work, droplets were printed with two different settings: droplet size small and medium. The final droplet size is determined by the properties of the ink (i.e., surface tension and viscosity), the nozzle diameter, the electric pulse shape driving the piezoelectric actuator in the printer head, the hydrophobicity of the substrate surface, etc. Additional printer settings were set as follows: high-resolution mode, unidirectional mode, single run (i.e., no repetition), and variable dot printing (VSD2), with a single droplet dispensing rate of ≤7.1 kHz. A color cartridge was used for the nanodiamond ink, which enabled access of up to 29 nozzles simultaneously (internozzle distance of 211.8 µm). Full details about the setup and systematics of droplet properties versus settings can be found in ref. [36]. Printing was done on diced pieces of natively oxidized Si wafer with dimensions of ≈4 × 1.5 cm^2, placed under the printer head onto a support built for the purpose.

Nanodiamond Ink: The nanodiamond ink was prepared by diluting the commercial NanoAmando (monodispersed detonation nanodiamond) colloid from NanoCarbon Research Institute Co. (Japan) with ultrasonicated deionized water from 50 g L^{-1} (stock concentration) to 2 g L^{-1}, similar to the procedure described in detail elsewhere.[39] The diluted solution was then injected into an empty clean printer cartridge with a syringe and installed in the printer.

Diamond Growth and Device Fabrication: After printing, the Si substrate was loaded into a home-built HFCVD chamber for the growth of a thin NCD layer from ≈100 nm up to ≈1.3 µm thickness. Growth conditions consisted of 725 °C, 10 mbar, with 1.5 to 6 sccm CH_4, and 300 sccm H_2. The diamond films were made suspended through underetching of the Si substrate by RIE, using an Adixen AMS-100 setup operating at 2000 W, no bias, 100 µbar working pressure, 500 sccm SF_6 gas and –10 °C stage temperature. A final acid cleaning step in boiling HCl (38%), H_2SO_4 (95%), and HNO_3 (70%) (1:1:1 volume ratio), followed by cleaning in boiling deionized water, was performed in order to remove residuals and particles left after RIE and surface contamination from air. Deposition of Au for mass sensing was performed by e-beam evaporation (Leybold L560) at 6 × 10^{-6} mbar, at a nominal deposition rate of 0.18 Å s^{-1} for a target thickness of 2.5 nm.

Structure and Morphology Characterization: SEM measurements were performed with a Jeol JSM-6010LA scanning electron microscope, at 5–15 keV and secondary electron detector, and with a field-emission FEI Nova NanoSEM 450 setup operating at 15 keV, with a high-resolution (immersion mode) secondary electron detector. Stitching of multiple SEM images was performed with ImageJ software. Raman spectroscopy measurements were performed with a Horiba LabRAM HR setup, equipped with an argon ion laser operating at 514 nm, and spectral resolution of ≈0.3 cm^{-1}. Height profile imaging of the patterned samples was performed with a Bruker Contour GT-K 3D optical microscope operating at highest (50–100×) magnification, with white light illumination, and VXI mode for better accuracy.

Vibrational and FEM Analyses: The frequency response of the NCD micro-disk resonators was measured by a home-built interferometry setup described in detail elsewhere.[60] In this system, the devices were mounted in a vacuum chamber (base pressure $P_{base} < 10^{-5}$ mbar), and actuated optothermally by a pulsed blue laser. A red laser was used for the readout of the deflection, and a vector network analyzer (VNA) was used to probe the frequency response. The vacuum chamber was also connected to a mass flow controller for optional measurements in controlled atmosphere with He, N_2, Kr, and SF_6. The damped/driven harmonic oscillator model was used to determine the resonance frequencies, f_0, and the quality factor, $Q = f_0/\gamma$, with γ being the damping constant, by nonlinear regression of the measured amplitude signals. Finite element method/modeling of the fabricated devices was performed with the MEMS module within COMSOL Multiphysics 5.2. Each NCD disk resonator was modeled according to its physical dimensions as measured by a combination of SEM, optical microscopy and optical profilometry measurements, taking into account also the shape of the supporting Si stem and the thicker NCD outer rim. The models were then fitted to the experimental data for the estimation of the NCD disk thickness, d, the density, ρ, the Young's modulus, E, and for the determination of the mode shapes.

Supporting Information

Supporting Information is available from the Wiley Online Library or from the author.

Acknowledgements

The authors thank the PME technical team, as well as Rick Waasdorp et al.[36] for the support with the inkjet setup. A.F.S. and J.G.B. thank the 3mE Faculty for the financial support through the Cohesion grant. R.J.D. and P.G.S. acknowledge this work as part of the research programme Integrated Graphene Pressure Sensors (IGPS) with project number 13307, which was financed by the Netherlands Organization for Scientific Research (NWO).

Note: Page 3, section 2.2, paragraph 2, line 4: "resonant" was updated to "resonance" on January 25, 2019 after initial online publication.

Conflict of Interest

The authors declare no conflict of interest.

Keywords

diamond, inkjet printing, mass sensors, micro-resonators, selective seeding

Received: September 13, 2018
Revised: November 9, 2018
Published online: December 19, 2018

[1] O. Auciello, S. Pacheco, A. V. Sumant, C. Gudeman, S. Sampath, A. Datta, R. W. Carpick, V. P. Adiga, P. Zurcher, Z. Ma, H. c. Yuan, J. A. Carlisle, B. Kabius, J. Hiller, S. Srinivasan, *IEEE Microw. Mag.* **2007**, *8*, 61.

[2] T. Yoshikawa, M. Reusch, K. Holc, D. Iankov, V. Zuerbig, A. Zukauskaite, C. E. Nebel, O. Ambacher, V. Lebedev, *Appl. Phys. Lett.* **2016**, *108*, 171903.

[3] R. Tabrizian, M. Rais-Zadeh, F. Ayazi, *TRANSDUCERS 2009-2009 Int. Solid-State Sensors, Actuators Microsystems Conf.*, IEEE, Piscataway, NJ **2009**, pp. 2131–2134.

[4] S. Stoupin, Y. V. Shvyd'ko, *Phys. Rev. B* **2011**, *83*, 104102.

[5] V. P. Adiga, A. V. Sumant, S. Suresh, C. Gudeman, O. Auciello, J. A. Carlisle, R. W. Carpick, *Phys. Rev. B* **2009**, *79*, 245403.

[6] N. Heidrich, D. Iankov, J. Hees, W. Pletschen, R. E. Sah, L. Kirste, V. Zuerbig, C. Nebel, O. Ambacher, V. Lebedev, *J. Micromech. Microeng.* **2013**, *23*, 125017.

[7] H. Najar, M.-L. Chan, H.-A. Yang, L. Lin, D. G. Cahill, D. A. Horsley, *Appl. Phys. Lett.* **2014**, *104*, 151903.

[8] T. L. Naing, T. O. Rocheleau, Z. Ren, S. S. Li, C. T. C. Nguyen, *J. Microelectromech. Syst.* **2016**, *25*, 11.

[9] V. Lebedev, T. Lisec, T. Yoshikawa, M. Reusch, D. Iankov, C. Giese, A. Žukauskaitė, V. Cimalla, O. Ambacher, *J. Micromech. Microeng.* **2017**, *27*, 065011.

[10] T. O. Rocheleau, T. L. Naing, Z. Ren, C. T. C. Nguyen, *2012 IEEE 25th Int. Conf. Micro Electro Mech. Syst.*, IEEE, Piscataway, NJ **2012**, pp. 672–675.

[11] M. Akgul, R. Schneider, Z. Ren, G. Chandler, V. Yeh, C. T.-C. Nguyen, *2011 Jt. Conf. IEEE Int. Freq. Control Eur. Freq. Time Forum Proc.*, IEEE, Piscataway, NJ **2011**, pp. 1–6.

[12] V. Lebedev, D. Iankov, N. Heidrich, V. Zuerbig, C. Wild, V. Cimalla, O. Ambacher, *J. Micromech. Microeng.* **2014**, *24*, 045015.

[13] F. Buja, A. V. Sumant, J. Kokorian, W. M. van Spengen, *Sens. Actuators, A* **2014**, *214*, 259.

[14] J. C. Arnault, *Carbon Nanoparticles and Nanostructures* (Eds: Y. Nianjun, X. Jiang, D.-W. Pang), Springer International Publishing, Basel, Switzerland **2016**, pp. 1–45.

[15] M. Possas, L. Rousseau, F. Ghassemi, G. Lissorgues, E. Scorsone, P. Bergonzo, *Microsyst. Technol.* **2016**, *22*, 609.

[16] R. Yang, C. A. Zorman, P. X.-L. Feng, *Diamond Relat. Mater.* **2015**, *54*, 19.

[17] M. Possas, L. Rousseau, F. Ghassemi, G. Lissorgues, P. Gonzales, E. Scorsone, P. Bergonzo, *Proc. Eng.* **2015**, *120*, 1115.

[18] R. Manai, E. Scorsone, L. Rousseau, F. Ghassemi, M. Possas Abreu, G. Lissorgues, N. Tremillon, H. Ginisty, J. C. Arnault, E. Tuccori, M. Bernabei, K. Cali, K. C. Persaud, P. Bergonzo, *Biosens. Bioelectron.* **2014**, *60*, 311.

[19] A. Bongrain, E. Scorsone, L. Rousseau, G. Lissorgues, P. Bergonzo, *Sens. Actuators, B* **2011**, *154*, 142.

[20] A. Bongrain, H. Uetsuka, L. Rousseau, L. Valbin, S. Saada, C. Gesset, E. Scorsone, G. Lissorgues, P. Bergonzo, *Phys. Status Solidi A* **2010**, *207*, 2078.

[21] F. Buja, J. Kokorian, A. V. Sumant, W. M. van Spengen, *Diamond Relat. Mater.* **2015**, *55*, 22.

[22] F. Buja, J. Kokorian, R. Gulotty, A. V. Sumant, W. M. van Spengen, *J. Micromech. Microeng.* **2015**, *25*, 125020.

[23] P. Calvert, *Chem. Mater.* **2001**, *13*, 3299.

[24] H. Sirringhaus, T. Kawase, R. H. Friend, T. Shimoda, M. Inbasekaran, W. Wu, E. P. Woo, *Science* **2000**, *290*, 2123.

[25] O.-S. Kwon, H. Kim, H. Ko, J. Lee, B. Lee, C.-H. Jung, J.-H. Choi, K. Shin, *Carbon* **2013**, *58*, 116.

[26] T. Öhlund, A. K. Schuppert, M. Hummelgård, J. Bäckström, H.-E. Nilsson, H. Olin, *ACS Appl. Mater. Interfaces* **2015**, *7*, 18273.

[27] K.-H. Choi, J. Yoo, C. K. Lee, S.-Y. Lee, *Energy Environ. Sci.* **2016**, *9*, 2812.

[28] A.-H. Alaaldeen, Q. Hala, A. Abdallah, A.-K. Jumana, *Sens. Rev.* **2018**, *38*, 438.

[29] M. Gao, L. Li, Y. Song, *J. Mater. Chem. C* **2017**, *5*, 2971.

[30] W. Su, B. S. Cook, Y. Fang, M. M. Tentzeris, *Sci. Rep.* **2016**, *6*, 35111.

[31] K. Yamada, T. G. Henares, K. Suzuki, D. Citterio, *Angew. Chem., Int. Ed.* **2015**, *54*, 5294.

[32] N. A. Fox, M. J. Youh, J. W. Steeds, W. N. Wang, *J. Appl. Phys.* **2000**, *87*, 8187.

[33] Y.-C. Chen, Y. Tzeng, A.-J. Cheng, R. Dean, M. Park, B. M. Wilamowski, *Diamond Relat. Mater.* **2009**, *18*, 146.

[34] Y.-C. Chen, Y. Tzeng, A. Davray, A.-J. Cheng, R. Ramadoss, M. Park, *Diamond Relat. Mater.* **2008**, *17*, 722.

[35] P. Kulha, J. Kroutil, A. Laposa, V. Procházka, M. Husák, *J. Electr. Eng.* **2016**, *67*, 61.

[36] R. Waasdorp, O. van den Heuvel, F. Versluis, B. Hajee, M. K. Ghatkesar, *RSC Adv.* **2018**, *8*, 14765.

[37] R. D. Deegan, O. Bakajin, T. F. Dupont, G. Huber, S. R. Nagel, T. A. Witten, *Nature* **1997**, *389*, 827.

[38] H. B. Eral, D. M. Augustine, M. H. G. Duits, F. Mugele, *Soft Matter* **2011**, *7*, 4954.

[39] M. Tsigkourakos, T. Hantschel, S. D. Janssens, K. Haenen, W. Vandervorst, *Phys. Status Solidi A* **2012**, *209*, 1659.

[40] R. Dufour, G. Perry, M. Harnois, Y. Coffinier, V. Thomy, V. Senez, R. Boukherroub, *Colloid Polym. Sci.* **2013**, *291*, 409.

[41] X. Chen, J. A. Weibel, S. V. Garimella, *Sci. Rep.* **2015**, *5*, 17110.

[42] J. G. Buijnsters, J.-P. Celis, R. W. A. Hendrikx, L. Vázquez, *J. Phys. Chem. C* **2013**, *117*, 23322.

[43] J. G. Buijnsters, M. Tsigkourakos, T. Hantschel, F. O. V. Gomes, T. Nuytten, P. Favia, H. Bender, K. Arstila, J.-P. Celis, W. Vandervorst, *ACS Appl. Mater. Interfaces* **2016**, *8*, 26381.

[44] A. Merlen, J. G. Buijnsters, C. Pardanaud, *Coatings* **2017**, *7*, 153.

[45] V. Podgursky, T. Hantschel, A. Bogatov, E. Kimmari, M. Antonov, M. Viljus, V. Mikli, M. Tsigkourakos, W. Vandervorst, J. G. Buijnsters, A. T. Raadik, P. Kulu, *Tribol. Lett.* **2014**, *55*, 493.

[46] A. C. Ferrari, J. Robertson, *Phys. Rev. B* **2000**, *61*, 14095.

[47] C. Zhao, M. H. Montaseri, G. S. Wood, S. H. Pu, A. A. Seshia, M. Kraft, *Sens. Actuators, A* **2016**, *249*, 93.

[48] M. K. Zalalutdinov, M. P. Ray, D. M. Photiadis, J. T. Robinson, J. W. Baldwin, J. E. Butler, T. I. Feygelson, B. B. Pate, B. H. Houston, *Nano Lett.* **2011**, *11*, 4304.
[49] G. Cicala, V. Magaletti, G. S. Senesi, G. Carbone, D. Altamura, C. Giannini, R. Bartali, *Mater. Chem. Phys.* **2014**, *144*, 505.
[50] S. Michael, S. Matthias, S. Thilo, H. Wilfried, K. Franz, *J. Phys.: Conf. Ser.* **2012**, *362*, 012033.
[51] M. Li, H. X. Tang, M. L. Roukes, *Nat. Nanotechnol.* **2007**, *2*, 114.
[52] W. E. Newell, *Science* **1968**, *161*, 1320.
[53] K. B. Gavan, J. van der Heijden, E. W. J. M. van der Drift, H. S. J. van der Zant, *2009 4th IEEE Int. Conf. Nano/Micro Eng. Mol. Syst.*, IEEE, Piscataway, NJ **2009**, pp. 380–384.
[54] V. Kara, V. Yakhot, K. L. Ekinci, *Phys. Rev. Lett.* **2017**, *118*, 74505.
[55] M. Bao, H. Yang, *Sens. Actuators, A* **2007**, *136*, 3.
[56] A. Cagliani, Z. J. Davis, *2009 IEEE Sensors*, IEEE, Piscataway, NJ **2009**, pp. 1317–1320.
[57] J. Chaste, A. Eichler, J. Moser, G. Ceballos, R. Rurali, A. Bachtold, *Nat. Nanotechnol.* **2012**, *7*, 301.
[58] Y. T. Yang, C. Callegari, X. L. Feng, K. L. Ekinci, M. L. Roukes, *Nano Lett.* **2006**, *6*, 583.
[59] A. F. Sartori, M. Fischer, S. Gsell, M. Schreck, *Phys. Status Solidi A* **2012**, *209*, 1643.
[60] R. J. Dolleman, S. J. Cartamil-Bueno, H. S. J. van der Zant, P. G. Steeneken, *2D Mater.* **2016**, *4*, 011002.